

Mixing of hot shocked plasma with cold gas in Nova YZ Ret 2020

SHARON MITRANI,¹ EHUD BEHAR,^{1,2} JEREMY J. DRAKE,³ MARINA ORIO,^{4,5} KIM PAGE,⁶ VALENTINA CANTON,⁵
JAN-UWE NESS,⁷ AND KIRILL SOKOLOVSKY^{8,9}

¹*Department of Physics, Technion, Haifa 32000, Israel*

²*MIT Kavli Institute for Astrophysics and Space Research, Massachusetts Institute of Technology, Cambridge, MA 02139, USA*

³*Lockheed Martin, 3251 Hanover Street, Palo Alto, CA 94304*

⁴*Department of Astronomy, University of Wisconsin, 475 N. Charter Str., Madison, WI 53706, USA*

⁵*INAF-Padova, vicolo Osservatorio 5, I-35122 Padova, Italy*

⁶*School of Physics and Astronomy, The University of Leicester, University Road, Leicester LE1 7RH, UK*

⁷*European Space Agency (ESA), European Space Astronomy Centre (ESAC), Camino Bajo del Castillo s/n, E-28692 Villanueva de la Cañada, Madrid, Spain*

⁸*Department of Astronomy, University of Illinois at Urbana-Champaign, 1002 W. Green Street, Urbana, IL 61801, USA*

⁹*Sternberg Astronomical Institute, Moscow State University, Universitetskii pr. 13, 119992 Moscow, Russia*

ABSTRACT

The origin of bright X-ray emission lines that appear late in a nova eruption remains largely a puzzle. We present two high-resolution X-ray grating spectra of the classical nova YZ Ret, observed 77 and 115 days post-eruption, using *XMM-Newton* and *Chandra*, respectively. Both spectra feature resolved emission lines blueshifted by $v = -1500 \text{ km s}^{-1}$ and broadened by $\sigma_v = 500 \text{ km s}^{-1}$. The two spectra are well described by a collisionally ionized plasma of $kT \sim 70 \text{ eV}$ that dimmed by a factor of ~ 40 between the two exposures. The spectra also show narrow radiative recombination continua (RRCs) of C^{+4} , C^{+5} , and N^{+5} , indicating the interaction of the hot ionized plasma with cold electrons of $kT \sim 2 \text{ eV}$. The high- n Rydberg series of C^{+4} is anomalously bright, allowing us to measure the electron density through continuum lowering, which is in agreement with the He-like N^{+5} density diagnostic of $n_e = (1.7 \pm 0.4) \times 10^{11} \text{ cm}^{-3}$. The high population of these high- n levels constitutes the best evidence to date of charge exchange (CX) with neutral H in an astrophysical ionized plasma. The remarkable fact that the velocity and plasma temperature are the same after 38 days, despite the high density and decreasing flux is evidence for ongoing heating. We suggest the heating is due to a reverse shock in the nova ejecta, which forms a thin X-ray shell. The narrow RRCs and CX are attributed to direct mixing with cold gas, which overtakes the hot plasma either from the shock front, or through the contact discontinuity.

1. INTRODUCTION

Classical and recurrent novae are interacting binary systems hosting a white dwarf (WD). Their eruptions are attributed to a thermonuclear runaway (TNR) in the atmosphere of the WD, which has been accreting material from its binary companion. Models predict that TNR is followed by a radiation driven wind, which depletes the accreted envelope (Starrfield et al. 2012; Wolf et al. 2013), or by a wind originating in the common envelope, most likely because of double Roche-lobe filling (see Shen & Quataert 2022).

Novae eruptions are luminous at all wavelengths, from γ -rays to radio. X-rays specifically provide an important window to understand their physics. Early in the nova eruption, the X-rays are attributed to powerful shocks in the outflow. Line-resolved X-ray grating spectra have been successfully described by collisional ionization steady-state models (see the discussions in Orio 2012; Drake et al. 2016; Peretz et al. 2016; Orio et al. 2020; Chomiuk et al. 2021). However, transient states occur early in the eruption (Orio et al. 2023; Islam & Mukai 2023). Nova shocks are powerful

enough that they can produce γ -ray emission (Franckowiak et al. 2018), of either leptonic (e.g., inverse Compton off of accelerated electrons) or hadronic origin (proton interactions producing neutral pions that emit γ -rays as they decay).

After a few days to almost a year, most novae transition to the supersoft phase, where the X-ray luminosity can exceed 10^{38} erg s $^{-1}$ (Eddington level for $\simeq 1 M_{\odot}$), with all the flux emitted below 0.8 keV (see review by Orio 2012). This happens because the WD atmosphere contracts at constant bolometric luminosity, so that the effective temperature keeps on increasing and the peak wavelength of the emission moves from the optical range, to the UV and extreme UV, and eventually to the soft X-rays within weeks. The source continues to be powered by shell burning. The central source appears as a *thermal* continuum X-ray supersoft source (SSS), with a peak temperature up to 10^6 K, for a time lasting from days to a few years (Yaron et al. 2005). The more massive the WD, the shorter is the SSS phase (Yaron et al. 2005; Starrfield et al. 2012; Wolf et al. 2013).

The 2020 nova YZ Ret discussed in this paper appeared to follow the trend of brightening and softening, as expected in the emergence of the SSS, however the X-ray luminosity remained much below the level of other novae (e.g. Orio et al. 2022). When the high resolution X-ray observations were triggered, quite surprisingly only an emission line spectrum was observed, with no sign of the WD continuum (SSS) (Sokolovsky et al. 2022). The SSS could be obscured by an accretion disk, indicating a high inclination system (Ness et al. 2013). In this paper, we analyze and discuss the puzzling X-ray spectra of the nova, at X-ray maximum flux and during the decay phase.

1.1. Nova outburst of YZ Ret

Nova YZ Ret nova erupted in a known binary with a WD. For a summary of previous observations, see Sokolovsky et al. (2022). It was discovered in outburst at 5th magnitude on 2020 July 15, and the optical maximum was later discovered to have occurred on 2020 July 11 at 3.7 mag (Kaufman et al. 2020). Hence, YZ Ret became visible with the naked eye and the second-brightest nova in a decade. Optical spectroscopic follow-up confirmed it to be a nova (Aydi et al. 2020). Kaufman et al. (2020) described the spectrum after the onset of the eruption as that of a Fe II-type nova (according to the classification scheme of Williams 1992), but Carr et al. (2020) reported a He/N-type on later days. There is now a common understanding that these are successive phases in the spectral evolution of novae (Aydi et al. 2023). From an overabundance of oxygen and prominent UV emission lines in the UV, Izzo et al. (2020) concluded that the nova erupted on an ONe WD. However, we find no oxygen in the X-ray spectrum.

An X-ray flash detected from YZ Ret immediately after the outburst was ascribed to the fireball phase, namely an early SSS phase of a few hours, when the nova is still undergoing the TNR (König et al. 2022). YZ Ret was detected in γ -rays (0.1-1 GeV) with *Fermi-LAT*, and in hard X-rays (3-79 keV) with *NuSTAR*, during its first two weeks. Sokolovsky et al. (2022) fitted the X-ray broad band spectra with unusual abundances from their model, namely a collisionally-ionized plasma either deficient in iron or overabundant in oxygen and nitrogen. They also showed the *XMM-Newton* high resolution grating spectrum, which is the focus of the present paper, but did not analyze it.

YZ Ret was classified as a VY Scl system (Sokolovsky et al. 2022, and references therein). VY Scl binaries were defined by Honeycutt & Kafka (2004) as cataclysmic variables undergoing fading of the optical light by 1.5 to 7 mag over less than 150 days, and these states recur over timescales from weeks to years. In the more common high state, VY Scl binaries have large optical and UV luminosity. This is interpreted as evidence that most of the time mass transfer onto the WD occurs at a rate $\dot{m} > 10^{-10} M_{\odot} \text{ yr}^{-1}$, necessary to sustain an accretion disc in a stable hot state in which dwarf novae outbursts are suppressed. The low states have been attributed to a sudden drop of \dot{m} from the secondary, or even to a total cessation of mass transfer (King & Cannizzo 1998; Hessman 2000), perhaps due to spots on the surface of the secondary covering the L1 point (Livio & Pringle 1994) or non-equilibrium of the irradiated atmosphere of the donor (Wu et al. 1995). Monitoring the X-ray emission of a few of these peculiar binaries, Zemko et al. (2014) ruled out non-explosive thermonuclear burning.

The observations included in this article were triggered after *Swift* XRT monitoring showed the emergence of a soft and luminous object, with the aim of studying the WD emission in the SSS phase. It was soon realized from *XMM-Newton* (Sokolovsky et al. 2022) and *NICER* spectra (Orio et al. 2022) that the X-rays from YZ Ret cannot be attributed to the WD. Detecting such soft X-ray flux from Galactic novae is not often possible due to Galactic column densities of $N_{\text{H}} > 10^{21} \text{ cm}^{-2}$. However, YZ Ret is at a Galactic latitude of -46° , with a low column density of only $N_{\text{H}} = 1.2 \times 10^{20} \text{ cm}^{-2}$ (Kalberla et al. 2005). The distance to the nova is fairly well determined with GAIA, as $2.5 \pm 0.3 \text{ kpc}$ (Bailer-Jones et al. 2021), which allowed to estimate its X-ray luminosity at a few $10^{35} \text{ erg s}^{-1}$. Indeed, this is an order of magnitude smaller than even the least luminous SSS-WD (generally, few $10^{36} \text{ erg s}^{-1}$ to few $10^{38} \text{ erg s}^{-1}$, Starrfield et al. 2012).

The two high resolution observations presented here confirm X-ray line emission with no photospheric SSS whatsoever. The SSS, thought to be the smoking gun of nuclear burning, has not been observed also in a few other novae and non-outbursting WD-SSS. [Ness et al. \(2013\)](#) explained the missing SSS with a non-disrupted (or quickly rebuilt) accretion disk in systems with high inclination. Notwithstanding, and as we show in the following sections, the spectra of YZ Ret are like no other, providing unprecedented insights into the atomic processes of shocked novae outflows. We describe the observations in [Sec. 2](#), the spectral diagnostic methods in [Sec. 3](#), and their rich application to the spectra in [Sec. 4](#). In [Sec. 5](#) we report global fits to the spectra. We discuss all of the results in [Sec. 6](#) and list our conclusions in [Sec. 7](#).

2. OBSERVATIONS

YZ Ret was monitored in outburst with the *Swift* X-ray Telescope (XRT, [Burrows et al. 2005](#)) over 155 days with a cadence that ranged from every 2 days to weekly monitoring. Two X-ray gratings observations of YZ Ret were triggered 77 and 115 days after the eruption; the first observation with the *XMM-Newton* Reflection Grating Spectrometers (RGS, [den Herder et al. 2001](#)), and the second one with the *Chandra* Low Energy Transmission Grating (LETG, [Brinkman et al. 2000](#)).

2.1. *Swift* XRT lightcurve

[Fig. 1](#) shows the XRT lightcurve featuring a rapid increase in count rate and a rapid decrease in hardness after day 50. At about day 90 the count rate started decreasing monotonically until day 160 when monitoring stopped. The RGS observation at day 77 caught the nova close to its highest state, while the LETG observation was carried out when the XRT count rate was more than an order of magnitude lower. Both grating spectra show a rich emission-line spectrum with no obvious continuum.

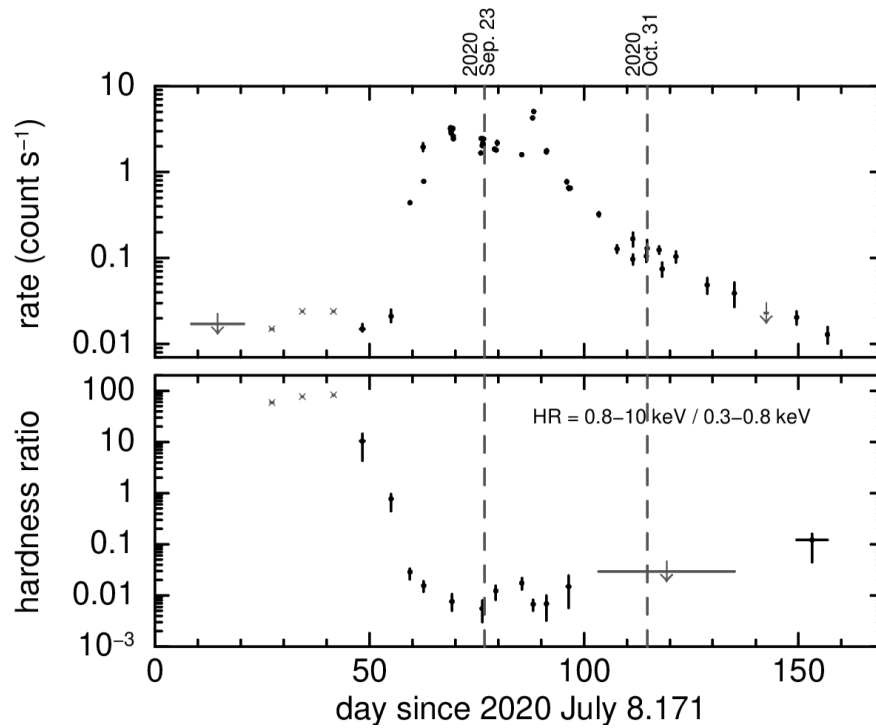


Figure 1. *Swift* XRT count rate (top panel) and hardness ratio (lower panel) measured in the first 155 days of the nova outburst. The vertical dashed lines indicate the observations of *XMM-Newton* (day 77) and *Chandra* (day 115). The observations obtained between days 27 and 42 were affected by high background emission below 0.5 keV. In these cases, the spectrum was fitted over 1-10 keV, and the model extrapolated down to 0.3 keV to estimate the count rate over the full 0.3-10 keV band. These data points are marked with x.

2.2. *XMM-Newton*/RGS spectrum

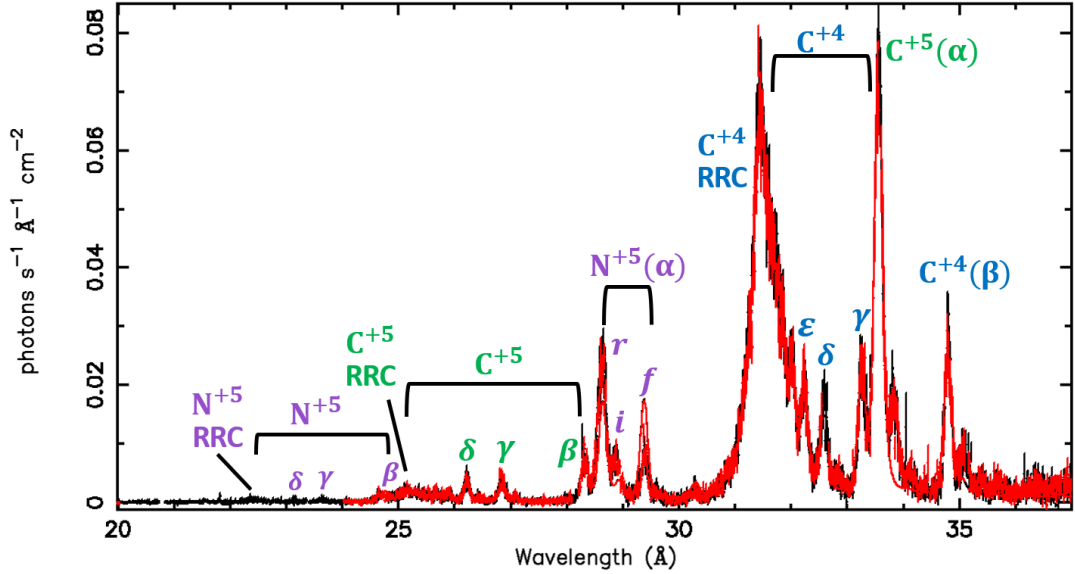


Figure 2. Fluxed spectrum of nova YZ Ret, observed in 2020-09-23 by *XMM-Newton*/RGS 77 days after the eruption. Black and red data are, respectively, RGS 1 and 2. Spectral lines of N^{+5} , C^{+4} , and C^{+5} are identified. The most prominent spectral feature is the narrow RRC of C^{+4} at 31.5 Å, along with the C^{+4} He series converging to it. The much fainter narrow C^{+5} RRC is just barely observed around 25.2 Å, along with the C^{+5} Lyman series. The N^{+5} RRC at 22.3 Å and its He series are also detected, and are shown more clearly in panel (a) of Fig.11.

Nova YZ Ret was observed with *XMM-Newton* 77 days after the initial eruption, between 2020-09-23 13:36 and 2020-09-23 21:22 UT (ObsID 0871010101; PI: K. Sokolovsky) for a total exposure time of 28 ks. The *Swift* XRT count rate during that week was around 2 cts s^{-1} , already close to its maximum. We use both RGS1 and RGS2 first-order spectra in the wavelength range of 5–37 Å, corresponding to the 0.33–2.5 keV energy range. We extracted the spectra with the XMM-SAS (XMM Science Analysis System) version 19.1¹ *rgsproc* task. Periods of high background were rejected. As explained in detail in Sokolovsky et al. (2022), we corrected the RGS spectra for pile up. Fig. 2 shows the spectra observed with RGS1 and RGS2.

2.3. *Chandra*/LETG spectrum

YZ Ret was observed with the *Chandra* LETG on 2020-10-31 for 31 ks. At the time of the YZ Ret eruption, the High Resolution Camera (HRC) aboard *Chandra* was not available in its HRC-S configuration, which is usually used with LETG (up to 175 Å). Instead, we used the HRC-I configuration to obtain a spectrum between 1.2 and 71 Å. The data were extracted with the *Chandra* CIAO data analysis package version 4.14.1 and the first-order grating redistribution matrix files and ancillary response files, using the CIAO task *chandra_repro*, with version 4.8.5 of the calibration package CALDB. We summed the positive- and negative- first order spectra with the *combine_grating_spectra* CIAO task, to increase the signal-to-noise ratio (S/N). We did not correct for the higher spectral orders, which have a negligible contribution. YZ Ret is by far fainter during this epoch than during the *XMM-Newton* observation. Fig. 3 shows the LETG spectrum.

3. DIAGNOSTIC METHODS FOR HIGH RESOLUTION SPECTRA

In order to properly model the rich line resolved spectra, we employ a collisional-radiative (CR) model. Assuming the ions are collisionally-ionized, excited by electrons, and in steady-state, the model computes level populations, and predicts the emission spectral line intensities (in units of $\text{ph s}^{-1} \text{cm}^{-3}$) associated with each transition between bound levels j and i ($j > i$) at the source

$$I_{ji} = n_j A_{ji} \quad (1)$$

¹ https://xmm-tools.cosmos.esa.int/external/xmm_user_support/documentation/sas.usg/USG.pdf

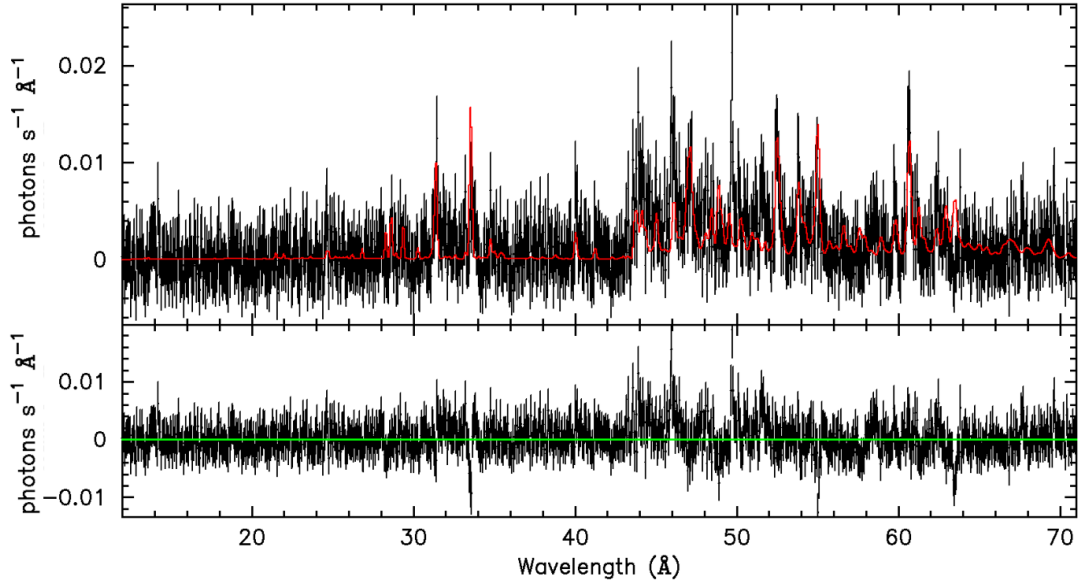


Figure 3. Spectrum of YZ Ret observed on 2020-10-31 for 31 ks with Chandra and the LETG+HRC-I instrumental setup. For clarity, given the low count rates, the spectrum is presented in photons (not flux), and with the fitted model (Sec. 5) to guide the eye. with residuals plotted in lower panel.

where n_j (cm^{-3}) is the number density of ions in level j and A_{ji} (s^{-1}) is the Einstein coefficient for spontaneous radiative decay. The level populations generally depend on electron density n_e and temperature T_e . At sufficiently high density, electron impact transitions between excited levels can change the relative populations (n_j in Eq. 1), hence the density sensitivity and diagnostics. The populations of all levels of a given ion are obtained by solving rate equations that include all of the processes that populate and depopulate each level (Mitrani & Behar 2023). Here, we add ionization and recombination processes. The atomic structure and coefficients were computed using the relativistic Hebrew University Lawrence Livermore Atomic Code (HULLAC, Bar-Shalom et al. 2001).

3.1. Narrow Radiative Recombination Continua (RRCs)

3.1.1. T_e Diagnostics

The free-bound transition of a plasma electron recombining with an ion emits a photon with an energy that equals the kinetic energy of the electron plus the ionization energy E_{ion} (of the recombined species). The emitted photons delineate the energy distribution of the electrons in the plasma, e.g., a Maxwell-Boltzmann (MB) distribution. Since the emitted photons have a sharp minimum energy of E_{ion} , the radiative recombination continuum (RRC) features a sharp edge at this energy, and usually a MB distribution thereafter:

$$f(E) = \begin{cases} 0, & E < E_{\text{ion}} \\ (C/kT_e)e^{-\frac{(E-E_{\text{ion}})}{kT_e}}, & E \geq E_{\text{ion}} \end{cases} \quad (2)$$

where C is a flux normalization factor.

In hot plasmas ($T_e > 10^5$ K), the RRC is significantly broadened by the temperature, and is hard to discriminate from other continua, primarily bremsstrahlung. When the plasma is colder ($T_e < 10^5$ K), narrow RRCs can be discerned in the spectrum, and their width provides exquisite T_e diagnostics. Narrow RRCs are routinely observed in photoionized plasmas (Liedahl & Paerels 1996; Kinkhabwala et al. 2002), where the electrons remain cold despite the high-energy ionizing photons and the high ionization degree of the plasma. However, narrow RRCs were also observed in a few hot, shocked X-ray sources, where no photo-ionizing continuum was observed nor expected (Schild et al. 2004; Nordon et al. 2009; Yamaguchi et al. 2009). In nova V4743 Sgr, a bright C^{+4} RRC was observed during the obscuration of the SSS (Ness et al. 2003, Fig. 4 therein), but not identified.

3.1.2. High- n Rydberg Series

When the RRC is sufficiently bright and narrow, and the resolution of the spectrometer sufficiently high, one can hope to resolve the Rydberg series of high- n (principal quantum number) emission lines converging onto the RRC. We are aware of one such observation to date (Nordon et al. 2009), and the second one is the present RGS spectrum of YZRet. If observed, this line series enables an interesting density diagnostic. The branching ratio for radiative decay from high- n levels, e.g., to the ground level (i.e., the observed X-ray line) is suppressed by collisional ionization, for which the rates increase with n . Thus, at some n_{\max} value, ionization dominates over line emission and the series is truncated. This effect of continuum lowering is known since the early days of quantum mechanics (Dewey & Robertson 1928; Inglis & Teller 1939). Since collisional ionization rates (S^{CI}) increase with n_e and radiative decays (A) do not, the observed n_{\max} , or equivalently the effective widening of the RRC edge, is a sensitive diagnostic of n_e :

$$\frac{A_{n_{\max}+1,1}}{S_{n_{\max}+1}^{CI}} < n_e < \frac{A_{n_{\max},1}}{S_{n_{\max}}^{CI}} \quad (3)$$

High- n levels are broadened by the Stark effect, which depends strongly on the plasma (ion) density. This makes the high order lines blend with the RRC above some n_{\max} that depends on ion density, assumed to be $\sim n_e$. Inglis & Teller (1939) give the following expression for the dependence of density on n_{max} in the Stark effect:

$$n_e = 0.027 n_{max}^{-7.5} a_0^{-3} \quad (4)$$

where $a_0 = 0.529 \times 10^{-8}$ cm is the Bohr radius.

3.2. He-like lines

The most common density diagnostic X-ray lines are those of the so-called He-like triplets, whose relative intensities depend on the density and temperature of the plasma (Gabriel & Jordan 1969). The three transitions from the 1s2s, 1s2p_{3/2}, and 1s2p_{1/2} $J = 1$ levels to the ground level 1s² ($J = 0$) are referred to, respectively, as the *forbidden* (f), *intercombination* (i), and *resonance* (r) lines. The 1s2s ($J = 1$) level is a meta-stable level with a relatively long life time. Hence, the line ratio

$$R(n_e) = \frac{f}{i} \quad (5)$$

is sensitive to n_e in a defined range where collisional de-excitation rates are comparable to the (low) decay rate A_{ji} from that level. These density ranges in He-like ions increase with the atomic number, as A_{ji} increases with the nuclear charge (Gabriel & Jordan 1969). Using the CR model we compute the expected ratios as a function of n_e , and infer the density by comparing with the measured ratio.

3.3. Emission Measure

The emitted flux from an optically thin uniform plasma is proportional to the emission measure $EM = \int n_e n_H dV \approx n_e n_H V$ where n_H (cm⁻³) is the hydrogen density, and V (cm³) is the volume of the emitting plasma. An EM can be obtained directly from discrete features, in this case the RRC photon luminosity $L_{RR} = n_q n_e \alpha^{RR} V$, where α^{RR} is the RR rate coefficient, and n_q is the number density of the recombining ion q . Since $n_q = f_q A_Z n_H$, the photon flux can be written as:

$$F^{RRC} = \frac{1}{4\pi d^2} f_q A_Z \alpha^{RR} EM \quad (6)$$

where f_q is the ion fraction, A_Z is the elemental abundance, and d is the distance to the source. In a hot collisionally-ionized plasma, where all photons are emitted following electron-ion collisions, the photon flux F is exactly proportional to the EM . Thus, by measuring the flux, one obtains the EM . In the Xspec (Arnaud 1996) model we use in Sec. 5 (*bvapec*, Smith et al. 2001), F is parameterized by:

$$F = \frac{10^{-14}}{4\pi d^2} EM \quad (7)$$

Once d is known, and the density is measured, the EM reveals the emitting volume V .

4. ANALYSIS OF XMM-NEWTON RGS SPECTRUM

The RGS spectrum allows us to derive the temperatures, densities, and EM of the X-ray source at day 77. The Lyman, and He series of C^{+5} and C^{+4} , as well as that of N^{+5} , are clearly identified, all blueshifted from their laboratory wavelengths. The predominant feature in the spectrum is the narrow RRC of C^{+4} around 31.5 \AA , which is broadened and asymmetric due to the electron temperature on the short-wavelength side, and the high- n lines on its long-wavelength side. Similar but much fainter features are the narrow C^{+5} and N^{+5} RRCs observed around 25.2 \AA and 22.3 \AA , respectively. The He-like triplet of N^{+5} is observed around 29 \AA , and the He-like triplet of C^{+4} is at 40 \AA outside the RGS band.

4.1. C^{+4} , C^{+5} and N^{+5} RRCs

A zoom into the C^{+4} RRC region between $30\text{--}33.5 \text{ \AA}$ is shown in Fig. 4, with the bright RRC blueshifted by $\sim 1500 \text{ km s}^{-1}$ and peaking at 31.45 \AA . We modeled this region with an RRC (Eq. 2) and a series of gaussians representing the Rydberg series. The RRC model provides a temperature measurement of $kT_{e,C^{+4}} = (1.96 \pm 0.04) \text{ eV}$. The series of unresolved C^{+4} lines are fixed to the theoretical wavelengths of the np to $1s$ transitions, and their Gaussian width to that of the global fit $\sigma_v = 520 \text{ km s}^{-1}$ (Sec. 5). Line intensities for $n \geq 10$ are scaled as n^{-3} , to follow the hydrogenic scaling of the Einstein coefficients. This is a good approximation for high- n levels, which are populated according to the Boltzmann distribution, and their close proximity implies comparable populations. The best fit to the spectrum is obtained when the highest level transition is $n_{\max} = 35$. In Fig. 5 (left panel), we plot the Cstat (C) fitting parameter as a function of n_{\max} , which demonstrates that $\Delta C_{\text{stat}} = 1$ corresponds to $n_{\max} = 35^{+10}_{-5}$. Performing the same fit with χ^2 yields $n_{\max} = 34^{+8}_{-5}$ with 90% confidence.

In order to measure n_e from n_{\max} , we need to scale A and S^{CI} with n (see Eq. 3). We extrapolated the HULLAC values for $n \geq 10$ according to $A_{n \rightarrow 1} \propto n^{-3}$, $S_{n \rightarrow \infty}^{CI} \propto n^2 \log(n)$ (Lotz 1968), which implies (c.f., Eq. 3):

$$n_e \simeq \frac{A_{n_{\max} \rightarrow 1}}{S_{n_{\max} \rightarrow \infty}^{CI}} \propto \frac{n_{\max}^{-5}}{\log(n_{\max})} \quad (8)$$

The inferred n_e from $n_{\max} = 35^{+10}_{-5}$ is $n_{e,RRC} = (2.4^{+3.0}_{-1.8}) \times 10^{11} \text{ cm}^{-3}$. Such high densities occur either in the dense blobs of ejecta, or in the accretion disk. Similarly high density has been found in Chandra X-ray grating spectroscopy of nova V959 Mon (Peretz et al. 2016).

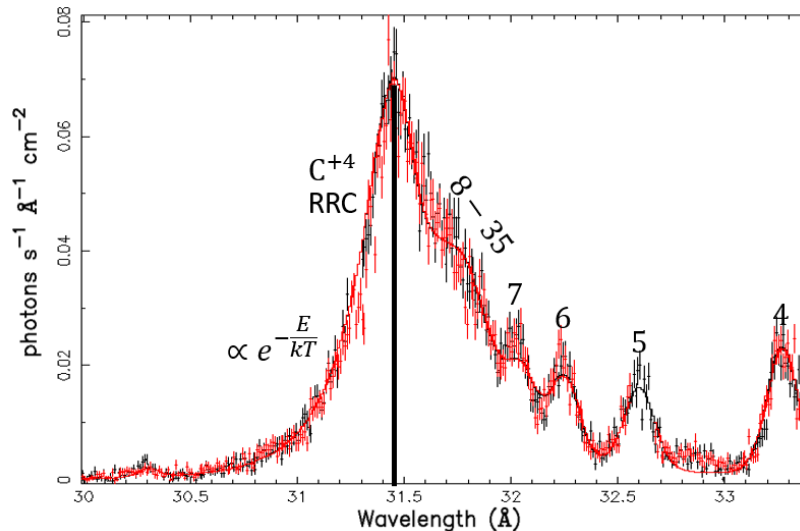


Figure 4. The 2020 RGS spectrum of YZ Ret in the range $30\text{--}33.5 \text{ \AA}$ highlighting the C^{+4} RRC region. Black and red data are RGS 1, and 2, respectively. The solid line is a model fitting the RRC, and the n to 1 Rydberg series up to n_{\max} as gaussians. The RRC exponential width on its blue side indicates $kT_{e,C^{+4}} = 1.96 \pm 0.04 \text{ eV}$. The best-fit n_{\max} is 35 (see Fig. 5).

The same diagnostics were applied to the C^{+5} RRC, which is observed at 25.2 \AA . The short-wavelength exponential profile yields a temperature measurement of $kT_{e,C^{+5}} = 1.9 \pm 0.2 \text{ eV}$, consistent with the C^{+4} temperature. The long-

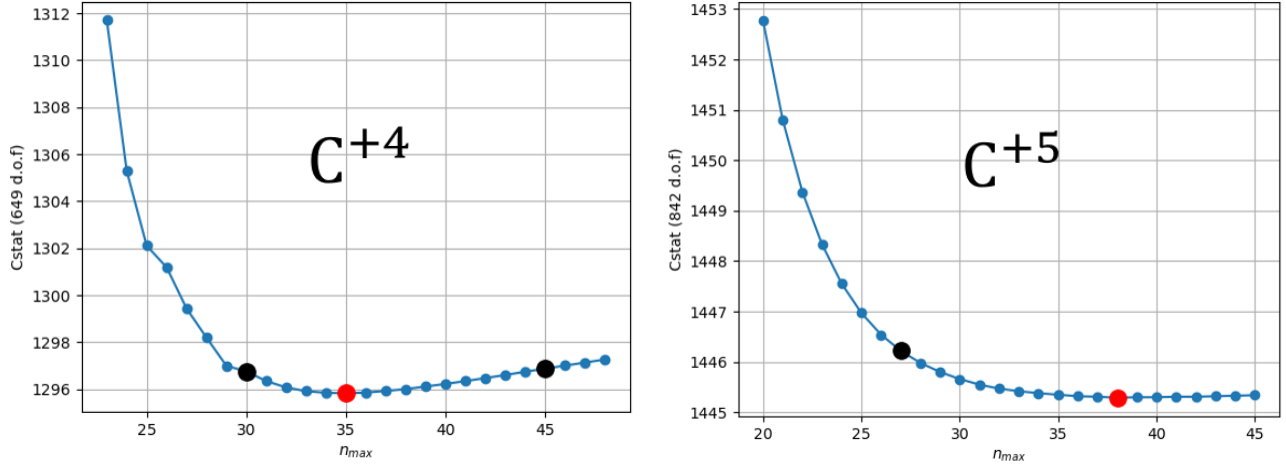


Figure 5. Values of C_{stat} obtained from fitting the Rydberg series up to n_{max} , the maximal $n \rightarrow 1$ transition included in the model for C^{+4} (left) and C^{+5} (right). The minimal C_{stat} value (red dot) and uncertainty region of $\Delta C_{\text{stat}} = 1$ (black dots) yield $n_{\text{max}} = 35_{-5}^{+10}$ for C^{+4} , and $n_{\text{max}} = 38 (> 27)$ for C^{+5} , which from Eq. 3 indicates an electron density of $n_{e,\text{RRC}} = (2.4_{-1.8}^{+3.0}) \times 10^{11} \text{ cm}^{-3}$ (for C^{+4}) and $n_{e,\text{RRC}} = (1.6 (< 9.6)) \times 10^{11} \text{ cm}^{-3}$ (for C^{+5}) at 90% confidence.

wavelength side of the C^{+5} RRC was fitted with a high- n levels series of Gaussians as the C^{+4} RRC yielding $n_{\text{max}} = 38$. Fig. 5 (right panel) shows that n_{max} can only be constrained from below $n_{\text{max}} > 27$. Using Eq. 8 we infer a density of $n_{e,\text{RRC}} < 9.6 \times 10^{11} \text{ cm}^{-3}$ (upper limit), with a best fit of $n_{e,\text{RRC}} = 1.6 \times 10^{11} \text{ cm}^{-3}$.

The same procedure was applied to the N^{+5} RRC, which only provides an upper limit of $kT_{e,\text{N}^{+5}} < 1.5 \text{ eV}$. The low flux of the N^{+5} RRC does not allow fitting of the high- n series and thus, no density diagnostic.

Interestingly, if we plug in the best constrained $n_{\text{max}} = 35$ from C^{+4} into the Stark-broadening density diagnostic (Eq. 4), we obtain $n_{e,\text{Stark}} = 4.8 \times 10^{11} \text{ cm}^{-3}$, which is within the uncertainties of the collisional continuum lowering estimate of Eq. 8. In summary, the RRCs of YZRet at day 77 indicate the presence of $kT_e \approx 2 \text{ eV}$ electrons with an electron density in the range of $1 - 5 \times 10^{11} \text{ cm}^{-3}$.

4.2. Charge Exchange

How exactly the high- n levels get so highly populated in YZRet and their lines so intense is an intriguing question. In fact, to the best of our knowledge, such a spectrum of C^{+4} has never been observed, including not in the laboratory. The high intensity of high- n lines is a smoking gun of charge exchange (CX). However, due to energy conservation, CX is highly selective in its population of excited levels. C^{+5} exchanging charge with a neutral H atom, both in the ground state, results primarily in C^{+4} ions in the $n = 4$ levels, with $n = 3, 5$ levels being appreciably less populated (Nolte et al. 2012). High collision velocities could result in somewhat higher levels, but equal fluxes of $n = 4 - 7$ lines and beyond as observed in Fig. 4 can not be explained by a high velocity alone. Conversely, CX with *excited* H atoms (or of excited C^{+5} in the initial state) requires much less energy to pull out the bound electron, and thus can end in higher- n levels of C^{+4} (e.g., Janev & Winter 1985). Since excited levels are close to each other, CX with H in (multiple) excited levels will populate a broader distribution of C^{+4} high- n levels, as observed here.

We therefore suggest CX in YZRet is occurring with excited H. At the measured electron density in the ionized gas of $n_e \approx 10^{11} \text{ cm}^{-3}$, $n = 2$ levels would be populated to 0.2% of the ground level. We have no measure of the neutral gas density, which could be denser than the ionized one. We conclude that the high- n lines of C^{+4} in the RGS spectrum of YZRet feature the first unambiguous, and most conspicuous evidence for CX in an astrophysical plasma (at least aside from the solar wind). Moreover, CX is completely in line with the observation of highly charged ions mixing with cold gas, as evident also by the RRCs.

4.3. He-like N^{+5} lines

In this section, we perform a direct measurement of the N^{+5} He-like line intensities, in order to infer the density of the plasma by using Eq. 5. Fig. 6 shows the three observed spectral lines of He-like N^{+5} , fitted with three Gaussians. The measured wavelength and flux of each line is presented in Table. 1, and the measured f/i ratio is $R(n_e)_{\text{N}^{+5}} = 1.1 \pm 0.2$ (Eq. 5). The average blueshift of the three lines is $v = -1620 \pm 80 \text{ km/s}$, which is slightly higher than the global fit

value in Sec. 5. The discrepancy can be due to an asymmetry of the r line, and $1s2l2l'$ satellite lines that blend with the N^{+5} lines, mostly the i line, similar to the $2l2l'$ satellites of C^{+5} at 33.85\AA (Sec. 4.4).

We solve the rate equations (Sec. 3) to obtain the theoretical ratio at $kT_e=2\text{ eV}$ (the cold recombining plasma component described in Sec. 4.1) and at 70 eV (the hot plasma component described in Sec. 5) to cover the expected temperature range. The computed f/i ratio as a function of n_e is presented in Fig. 7. The measured value of $R(n_e)_{N^{+5}} = 1.1 \pm 0.2$ indicates $n_e = (1.7 \pm 0.4) \times 10^{11}\text{ cm}^{-3}$, and $n_e = (5.8 \pm 0.7) \times 10^{10}\text{ cm}^{-3}$ for 2 eV and 70 eV , respectively. If satellite lines indeed blend with the i line, $R(n_e)$ is likely higher and the density is slightly lower (Fig. 7). The density for 2 eV is consistent with the value we obtained from n_{max} at the RRC $n_{e,RRC} = (2.4_{-1.8}^{+3.0}) \times 10^{11}\text{ cm}^{-3}$, and a factor 3 higher than the 70 eV value. The above measurement does not include photo-excitation (PE) because there is no observed continuum in the YZ Ret spectra.

We check whether the gas may be photo-ionized and PE processes could dramatically change our density measurement. The unobserved ionizing source we hypothesize is a continuum black body with a temperature of $kT_{bb}=50\text{ eV}$ and a luminosity of $L = 10^{38}\text{ erg s}^{-1}$, high but typical for a SSS. In photo-ionization steady state, the PE flux and n_e are related through the ionization parameter $\xi = L/(n_e r^2)$, where r is the distance from the ionizing source to the emitting plasma. N^{+5} typically forms at $\xi = 10\text{ erg s}^{-1}\text{ cm}$ (Kallman et al. 2009). Adding PE processes slightly reduces the density by 20%; at $kT_e = 2\text{ eV}$, $n_e = (1.4 \pm 0.4) \times 10^{11}\text{ cm}^{-3}$. $\xi = 10\text{ erg s}^{-1}\text{ cm}$ then implies $r = (7.6 \pm 0.9) \times 10^{12}\text{ cm}$. The outflow moving at 1500 km s^{-1} will reach a much larger distance at its observed age of 77 days. In addition, the second observation by *Chandra* shows the outflow at a similar ionization degree, which would be different if it moved away and was photo-ionized by the same SSS flux (see discussion in Sec. 6).

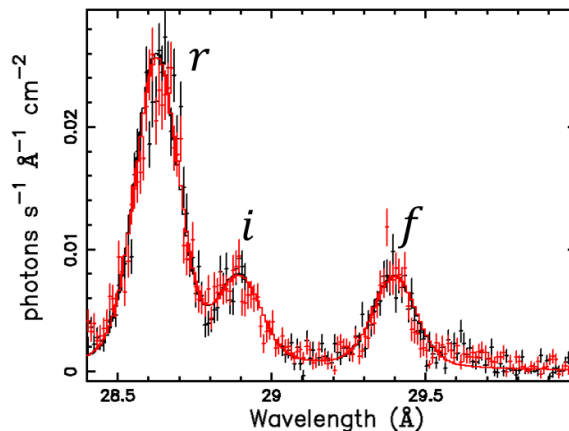


Figure 6. The r, i, f lines of N^{+5} observed in the YZ Ret RGS spectrum. The measured f/i ratio is 1.1 ± 0.2 .

Table 1. Measurements of the three He-like N^{+5} $n = 2 \rightarrow 1, J = 1 \rightarrow 0$ transitions. The average blueshift velocity is $v = -1620 \pm 80\text{ km/s}$.

Line	Transition	$\lambda_{\text{meas.}}[\text{\AA}]$	$\lambda_{\text{rest}}^{(a)}[\text{\AA}]$	$\Delta\lambda[\text{\AA}]$	Velocity [km/s]	Flux [$10^{-3}\text{ ph s}^{-1}\text{ cm}^{-2}$]
r	$1s2p_{1/2} \rightarrow 1s^2$	28.63 ± 0.01	28.787 ± 0.001	-0.15 ± 0.01	-1640 ± 100	(5.5 ± 0.2)
i	$1s2p_{3/2} \rightarrow 1s^2$	28.91 ± 0.02	29.081 ± 0.001	-0.17 ± 0.02	-1760 ± 210	(1.4 ± 0.2)
f	$1s2s \rightarrow 1s^2$	29.39 ± 0.01	29.534 ± 0.001	-0.14 ± 0.01	-1460 ± 100	(1.6 ± 0.2)

NOTE—

(a) Cann & Thakkar (1992); Drake (1969, 1971), taken from the NIST atomic database

4.4. Dielectronic recombination satellites

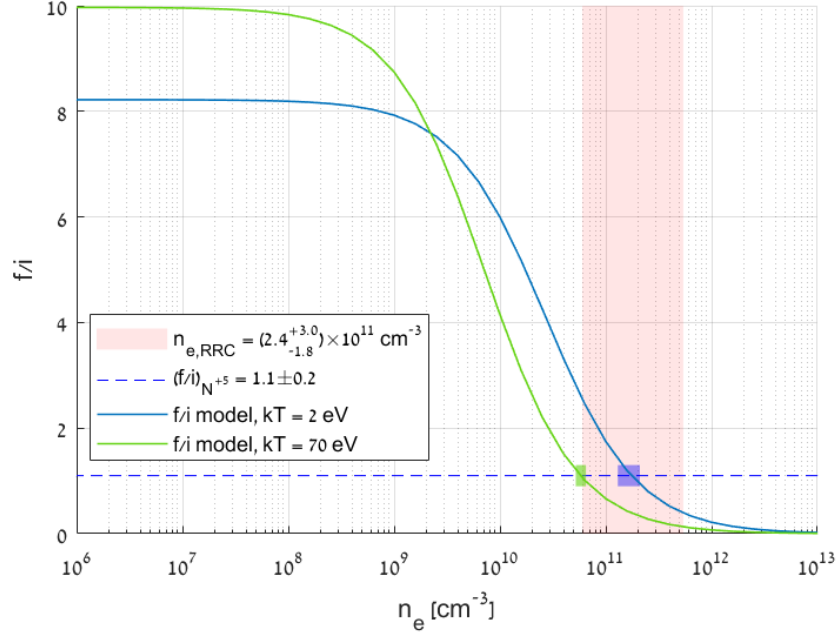


Figure 7. Computed f/i ratio as a function of n_e for $kT_e = 2$ eV (blue) and 70 eV (green). The blue dashed line is the measured f/i ratio in the spectrum. Shaded areas indicate uncertainties. The measured ratio indicates a density of $n_e = (1.7 \pm 0.4) \times 10^{11} \text{ cm}^{-3}$, for 2 eV, fully consistent with $n_{e,RRC} = (2.4^{+3.0}_{-1.8}) \times 10^{11} \text{ cm}^{-3}$ (Sec.4.1), which is represented by the red shaded area.

Prominent dielectronic recombination (DR) satellite lines of C^{+4} between 33.8–34.4 Å, and of C^{+3} between 35–35.8 Å are observed in the RGS spectrum of YZRet (Fig.8, panel (e) of Fig. 11). These lines exist in the hot collisional component (*bvapec*), but are by far weaker than the observed intensities. The same DR satellites are seen in laboratory plasma, such as laser-produced plasma (Seely et al. 1981), where the electron density exceeds $n_e \simeq 10^{20} \text{ cm}^{-3}$. In that case, one observes 1s-2p transitions produced by the $2p2l'$ and $2p3l'$ doubly excited levels decaying to $1sn'l'$, at wavelengths above and below 34 Å, respectively (c.f. Fig.3 in Seely et al. 1981). In contrast, in the present YZRet spectrum, n_e is much lower, and the $2l3l'$ lines are much brighter than the dim $2l2l'$ lines (Fig. 8). These DR satellites are all about 300 eV above the 1s continuum (see energy diagram in Fig. 9, left panel). Therefore, as the temperature approaches $kT \simeq 100$ eV, which is sufficient for dielectronic capture, they should all be populated, and appear in the spectrum. The weakness of the $2l2l'$ DR resonances above 34 Å in the YZRet spectrum compared to the bright $2l3l'$ ones just below 34 Å beg for an explanation.

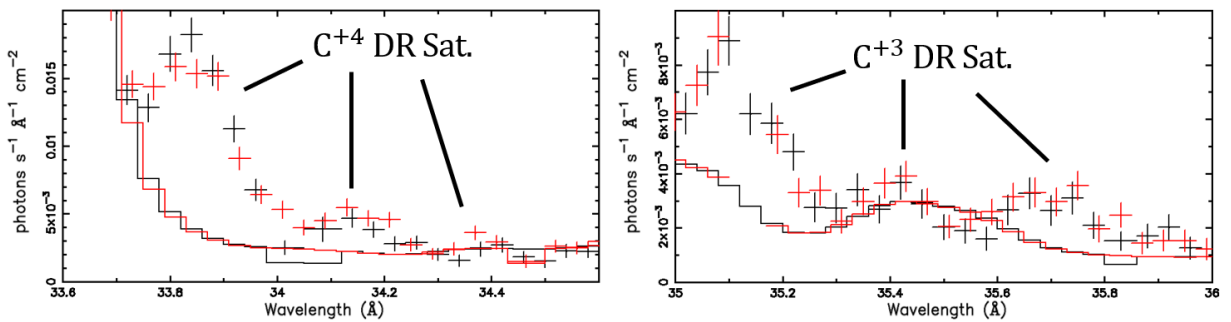


Figure 8. Dielectronic recombination satellite lines of C^{+4} and C^{+3} observed in the RGS 1 and 2 (black, red) spectrum, much above the plasma model prediction (solid line). The data were rebinned for clarity. The C^{+3} satellite lines (right panel) may be blended with Ca^{+10} or Ar^{+8} lines.

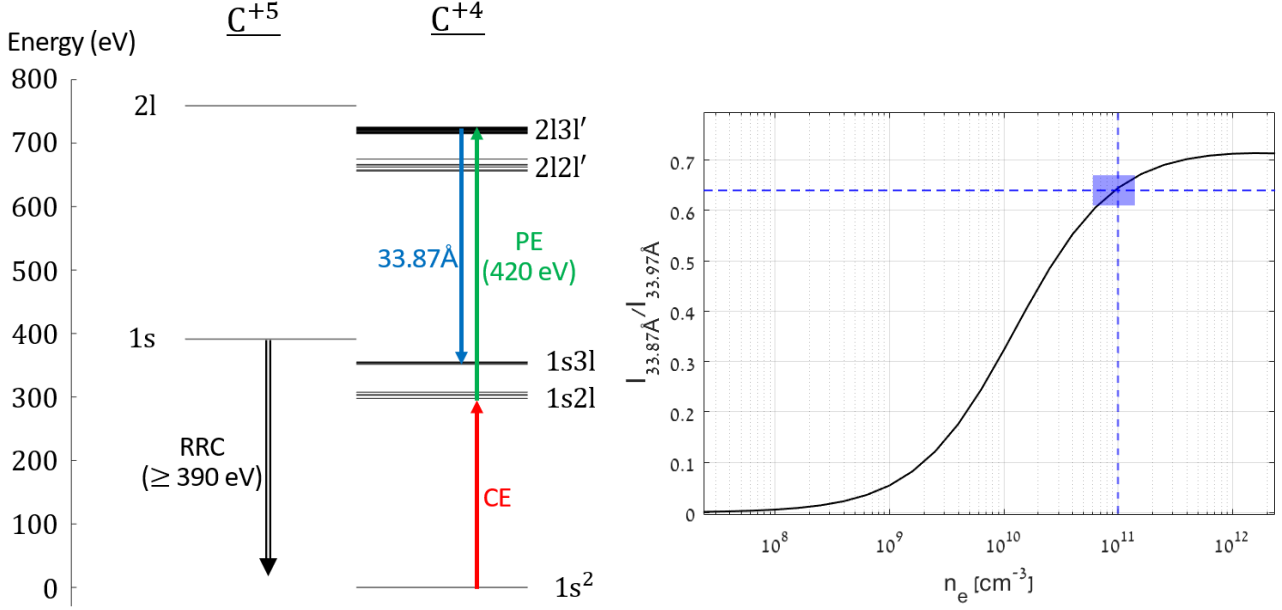


Figure 9. **Left:** Energy diagram of the C^{+5} & C^{+4} levels that are included in the CR model. Ions are excited by CE (red arrow), and further by PE (green arrow) selectively to the $2l3l'$ configuration complex, by C^{+4} RRC photons of 392-420 eV (29.5-31.6 Å). The ions decay to $1s3l$ levels, which produce the 33.87 Å satellite line (blue arrow) that is shown in Fig. 10 and in the observed YZ Ret spectrum (Fig. 8). **Right:** Intensity ratio of the 33.87 Å satellite line and C^{+4} He β at 33.97 Å, as a function of n_e . Since the population of the $1s2l$ levels depends on n_e , the line ratio provides a density diagnostic of $n_e = (1.0 \pm 0.4) \times 10^{11} \text{ cm}^{-3}$, consistent with the other density measurements (Sections 4.1, 4.3).

The peculiar satellites intensity ratios can be explained by a different mechanism than DR, which is *selective* PE photo-pumping from the $1s2l$ levels to the $2l3l'$ levels, by the intense C^{+4} RRC flux in the narrow band of 392-420 eV (29.5-31.6 Å, Fig. 11, panel (d)). This selective photo-pumping to $2l3l'$ explains why the lower $2l2l'$ levels are not populated (Fig. 9, left panel). For this mechanism to operate, the $1s2l$ levels need to be sufficiently populated, namely n_e needs to be sufficiently high. At a density of $n_e \simeq 10^{11} \text{ cm}^{-3}$, the $1s2s$ ($J=1$) excited level is populated to 0.2% of the ground level by CE processes, to be subsequently photo-excited to the $2l3l'$ doubly excited levels. The density dependence of the population of this level provides another diagnostic, pointing yet again to $n_e \simeq 10^{11} \text{ cm}^{-3}$, see right panel of Fig. 9. The diagnostic was done with the line ratio of 33.87 Å (satellite)/33.97 Å ($C^{+4}\beta$), but it's not exclusive to the $C^{+4}\beta$ line. The ratio of the satellite line to C^{+5} Ly α can also be used as a density diagnostic, because the density affects the population of the $1s2l$ (for C^{+4}) and $2l$ (for C^{+5}) in a similar way. The correct line ratios are obtained in our model for a density of $n_e = (1.0 \pm 0.4) \times 10^{11} \text{ cm}^{-3}$, in agreement with the density measurements in Sections 4.1, 4.3.

The resulting synthetic spectrum of the $kT = 70 \text{ eV}$ CR model is shown in Fig. 10. The model includes the DR of C^{+5} via the doubly excited $2l2l'$ and $2l3l'$ configuration complexes, with an addition of photo-exciting flux, with the spectrum of the cold C^{+4} RRC between 392-420 eV. The spectrum in Fig. 10 was computed at $n_e = 10^{11} \text{ cm}^{-3}$, and matches the intensities of the satellite lines observed in YZ Ret.

The presence of a strong satellite line at 33.87 Å, along with the absence of strong matching satellite lines at 33.5 Å and 33.67 Å (rest frame) thus shows an interaction between the hot (70 eV) and cold (2 eV) components of the plasma. The RRC photon flux that is required for PE by the CR model in order to produce the correct intensities of the satellite lines is $F_{\text{RRC}} = 10^{28} \text{ ph s}^{-1} \text{ cm}^{-2}$. From the distance to YZ Ret of $d = 7.8 \times 10^{21} \text{ cm}$ away (Bailer-Jones et al. 2021), we know the RRC luminosity L_{RRC} . If this was a point source, the distance r from it at which $F_{\text{RRC}} = L_{\text{RRC}}/(4\pi r^2)$ is $r = 10^7 \text{ cm}$. This small distance is consistent with the physical picture of a thin shock-heated layer that is discussed in Sec. 6.2, where the ions mix with the cold electrons.

4.5. Volume and mass of the emitting plasma

In this section, we use the best-fitted fluxes of the (mixed) cold (RRCs) and hot (Sec. 5) plasmas listed in Table 2, to infer their volume from the density measurement (Eqs. 6, 7). In all the calculations, we use a distance to YZ Ret of

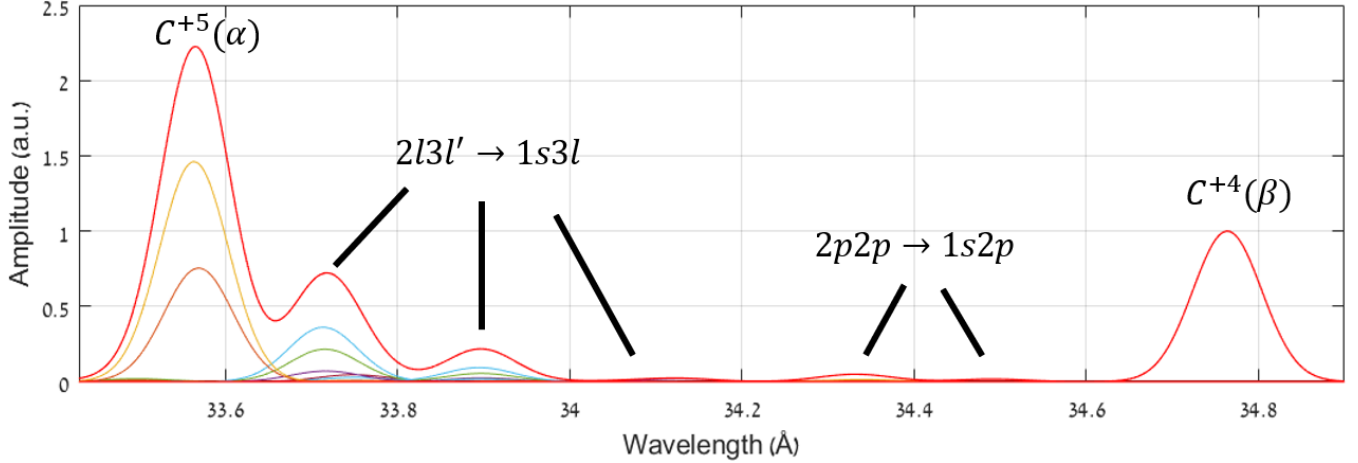


Figure 10. Synthetic spectrum produced by C^{+5} & C^{+4} CR model with $kT = 70$ eV, and $n_e = 10^{11} \text{ cm}^{-3}$, including DR via the doubly excited $2l2l'$ and $2l3l'$ configuration complexes, with an addition of PE. The colored lines are the individual transitions while the red line is their sum, which shows line ratios that match the observed spectrum of YZ Ret. The spectrum is blueshifted by $v = -1500 \text{ km s}^{-1}$

$d = (7.8 \pm 0.7) \times 10^{21} \text{ cm}$ (Bailer-Jones et al. 2021), a solar carbon abundance of $A_C = 4 \times 10^{-4}$ (Wilms et al. 2000), and the density value we obtained in Sec. 4.3, $n_e = (1.7 \pm 0.4) \times 10^{11} \text{ cm}^{-3}$.

For the cold plasma, we use the radiative recombination rate coefficients at 2 eV, $\alpha_{C^{+5}}^{RR} = 2.33 \times 10^{-12} \text{ cm}^{-3} \text{ s}^{-1}$ and $\alpha_{C^{+6}}^{RR} = 3.15 \times 10^{-12} \text{ cm}^{-3} \text{ s}^{-1}$ (computed by HULLAC) in Eq. 6 to obtain $f_{C^{+5}}V = (8 \pm 4) \times 10^{35} \text{ cm}^3$ and $f_{C^{+6}}V = (1.2 \pm 0.6) \times 10^{34} \text{ cm}^3$. If we assume the C^{+4} and C^{+5} RRCs are emitted from the same volume, then we can infer the ion fraction ratio $f_{C^{+6}}/f_{C^{+5}} = (1.5 \pm 0.9)\%$, meaning the carbon in the plasma is dominated by the C^{+5} ion ($f_{C^{+5}} \simeq 1$), which is consistent with the ionization balance of a hot plasma at a temperature of $kT_e \simeq 70$ eV. Finally, we obtain a volume of $V_{\text{cold}} = (8 \pm 4) \times 10^{35} \text{ cm}^3$.

The volume of the hot plasma (*bvapec* model) is obtained from Eq. 7, by assuming the standard $n_e/n_H = 1.2$ density ratio for a fully ionized, solar abundance plasma. If the hydrogen abundance is different than solar, one needs to introduce a correction factor (Leahy et al. 2023). We obtain $V_{\text{hot}} = (6 \pm 3) \times 10^{35} \text{ cm}^3$, which is consistent with V_{cold} , again lending to the notion that the hot and cold plasmas are mixed. Given the volume and density, we can estimate the mass in the X-ray source as $M = \mu m_p n_e V$, where $\mu m_p = 1.3 m_p$ is the mean atomic mass in the plasma, m_p being the proton mass. This estimate yields $M = 10^{-10} M_{\odot}$, which is fitting for such a low luminosity source. In Sec. 6 we show that the mass outflow rate is normal, but that the short cooling times leave only a small mass of hot gas at any given time.

5. GLOBAL FITTING

5.1. XMM-Newton/RGS

We zoom into the *XMM-Newton* RGS spectrum (Fig. 2) with five panels in Fig. 11. The best-fitted model (solid line in the figure) is a low-density, collisionally-ionized plasma model with varying abundances. The C abundance is set the unity. This is complemented by the RRCs and high- n line series of Sec. 4.1. In Xspec (Arnaud 1996), the *bvapec* component (Smith et al. 2001) represents an outflowing ($v = -1504 \pm 12 \text{ km s}^{-1}$) collisionally ionized plasma at $kT_e = 73 \pm 1$ eV, with lines kinematically broadened by $\sigma_v = 520 \pm 4 \text{ km/s}$. Three *redge* components represent the colder ~ 2 eV RRCs of C^{+4} , C^{+5} , and N^{+5} . The series of *agauss* Gaussian lines represent the high- n lines converging to the C^{+4} and C^{+5} RRCs (Sec. 4.1). The model also includes a Galactic absorption *tbabs* component with $N_H = 1.24 \times 10^{20} \text{ cm}^{-2}$ (Kalberla et al. 2005).

The hot plasma model (red dotted line in Fig. 12) tightly constrains the outflow velocity and plasma temperature, yields the abundances of N, Ca, and provides an upper limit for the O abundance (see Table 3). However, it cannot produce the RRCs, the high-order line series (black dotted lines in Fig. 12), or the DR satellite lines. More specifically, the observed intensities of the Lyman and Helium line series of C^{+5} and C^{+4} are by far stronger in the spectrum than their hot-plasma values, starting already from $n = 4$ (γ) and up to much higher and unresolved n values. These series

can be seen in panels (b) and (d) of Fig.11, where the hot plasma model has been appreciably enhanced with a series of Gaussians as in Sec.4.1. The DR satellites of C^{+4} and C^{+3} are observed, respectively, between 33.8-34.4 Å and between 35-35.8 Å (panel (e) of Fig.11), and are also not nearly as strong in the model. These lines are calculated separately in Sec.4.4 (Fig.8). Finally, the relative intensities of the $He\alpha$ N^{+5} lines observed between 28.6-29.4 Å (panel (c) of Fig.11) and of $He\beta$ at 24.76 Å (panel (b) of Fig.11) are inconsistent with the model intensities, due to its low density approximation (Sec.4.3).

5.2. Chandra/LETG

YZRet was observed with the *Chandra* LETG (Fig.13), 38 days after the RGS observation. The LETG extends the RGS waveband (up to 37Å) to 71Å, but the source at this stage was much fainter. We fitted the LETG spectrum with a similar model to that of the RGS. As in the RGS spectrum, the prominent features in the LETG spectrum are the C^{+4} RRC and the thermal line emission. The C^{+5} RRC and high- n lines are present, but too faint to be fitted.

The *bvapec* component represents an outflowing ($v = -1468 \pm 90$ km s $^{-1}$) collisionally-ionized plasma at $kT_e = 65 \pm 5$ eV. The kinematic broadening can not be constrained and fixed to the RGS best-fit value $\sigma_v = 520$ km/s. The RRC of C^{+4} indicates a cold temperature of $kT_e < 2.1$ eV. The softer spectrum of LETG allows us to constrain the abundances of Mg, Si, S, Ar, and Fe that were not available with the RGS. The measured parameters from RGS and LETG fitted spectra are compared in Tables 2, 3.

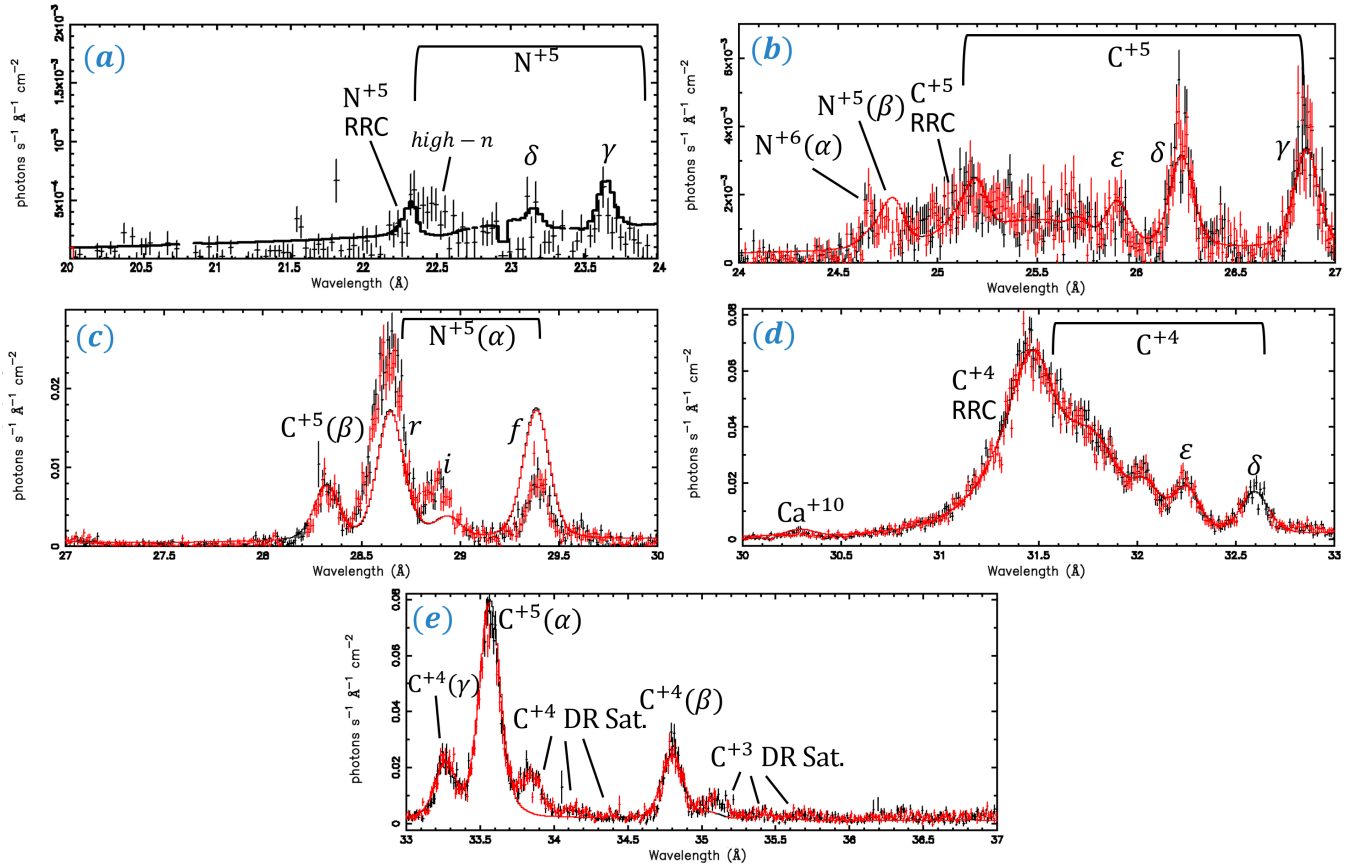


Figure 11. The full spectrum of YZ Ret observed by *XMM-Newton* RGS 1 (black) and RGS 2 (red) in the range of 20-37Å. The spectrum shows emission lines of several ions such as C^{+4} , C^{+5} , N^{+5} , N^{+6} , and Ca^{+10} . The solid line represents the fitted model of a velocity broadened collisionally ionized plasma (*bvapec*) with 3 colder RRC components for C^{+4} , C^{+5} and N^{+5} (*redge*), along with a series of gaussians to correct the amplitudes of the C^{+4} and C^{+5} high- n transitions (*agauss*). Note that the y-axis scale of the different panels is not the same.

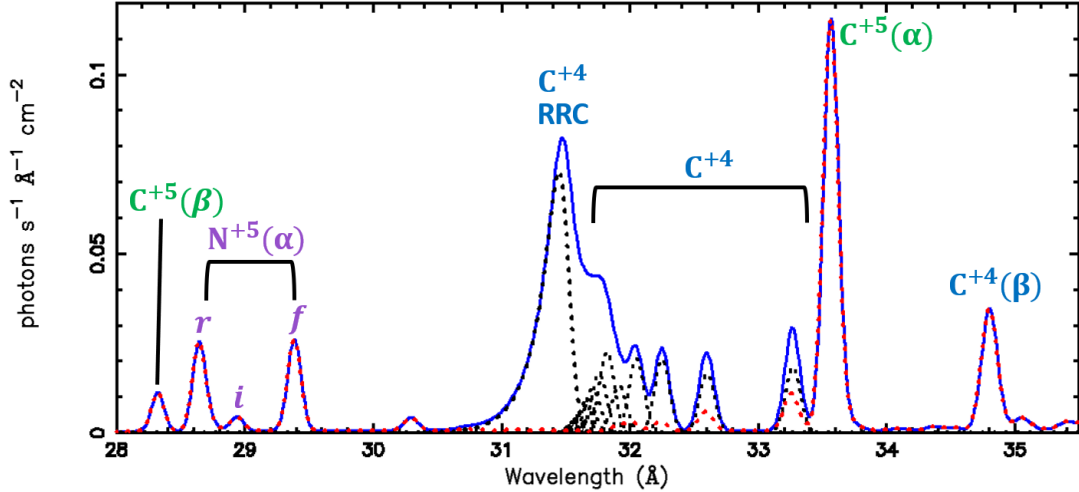


Figure 12. Theoretical model for the RGS spectral range of 28-35.5 Å. The hot component (*bvapec*) is plotted in (dotted) red. The RRC and the Rydberg series, which arise from the mixing with the cold medium, are plotted in (dotted) black, and the total in (solid) blue.

Table 2. Best-fit spectral parameters obtained from *XMM-Newton* RGS and *Chandra* LETG.

Observation	Component	Temperature [eV]	Velocity [km/s]	σ_v [km/s]	Flux [10^{-3} ph s $^{-1}$ cm $^{-2}$]	Volume [10^{35} cm 3]
<i>XMM-Newton</i> RGS	<i>bvapec</i>	73 ± 1	-1504 ± 12	520 ± 4	$(184 \pm 2)^{(a)}$	(6 ± 3)
	$C^{+4}RRC$	1.96 ± 0.04	"	"	(24.2 ± 0.4)	(8 ± 4)
	$C^{+5}RRC$	1.9 ± 0.2	"	"	(0.5 ± 0.05)	-
	$N^{+5}RRC$	< 1.5	"	"	(0.05 ± 0.02)	-
<i>Chandra</i> LETG	<i>bvapec</i>	65 ± 5	-1468 ± 90	"	$(4.4 \pm 0.5)^{(a)}$	(50 ± 20)
	$C^{+4}RRC$	< 2.1	"	"	(0.9 ± 0.3)	-

NOTE—(a) Measured in the range of 0.3-0.7 keV

Table 3. Elemental abundances of the hot gas relative to solar (Wilms et al. 2000) as measured by the *bvapec* model. Unlisted elements are not observed and were taken at solar values.

Element	<i>XMM-Newton</i> RGS	<i>Chandra</i> LETG
C	1.00	1.00
N	0.81 ± 0.03	0.7 ± 0.4
O	$< 5 \times 10^{-4}$	< 0.2
Mg	-(a)	1.5 ± 0.6
Si	-(a)	1.1 ± 0.4
S	-(a)	1.7 ± 0.4
Ar	-(a)	1.5 ± 0.4
Ca	1.2 ± 0.1	< 6.6
Fe	-	4.0 ± 3.3

NOTE—(a) Set to the values obtained by the *Chandra* fitted spectrum.

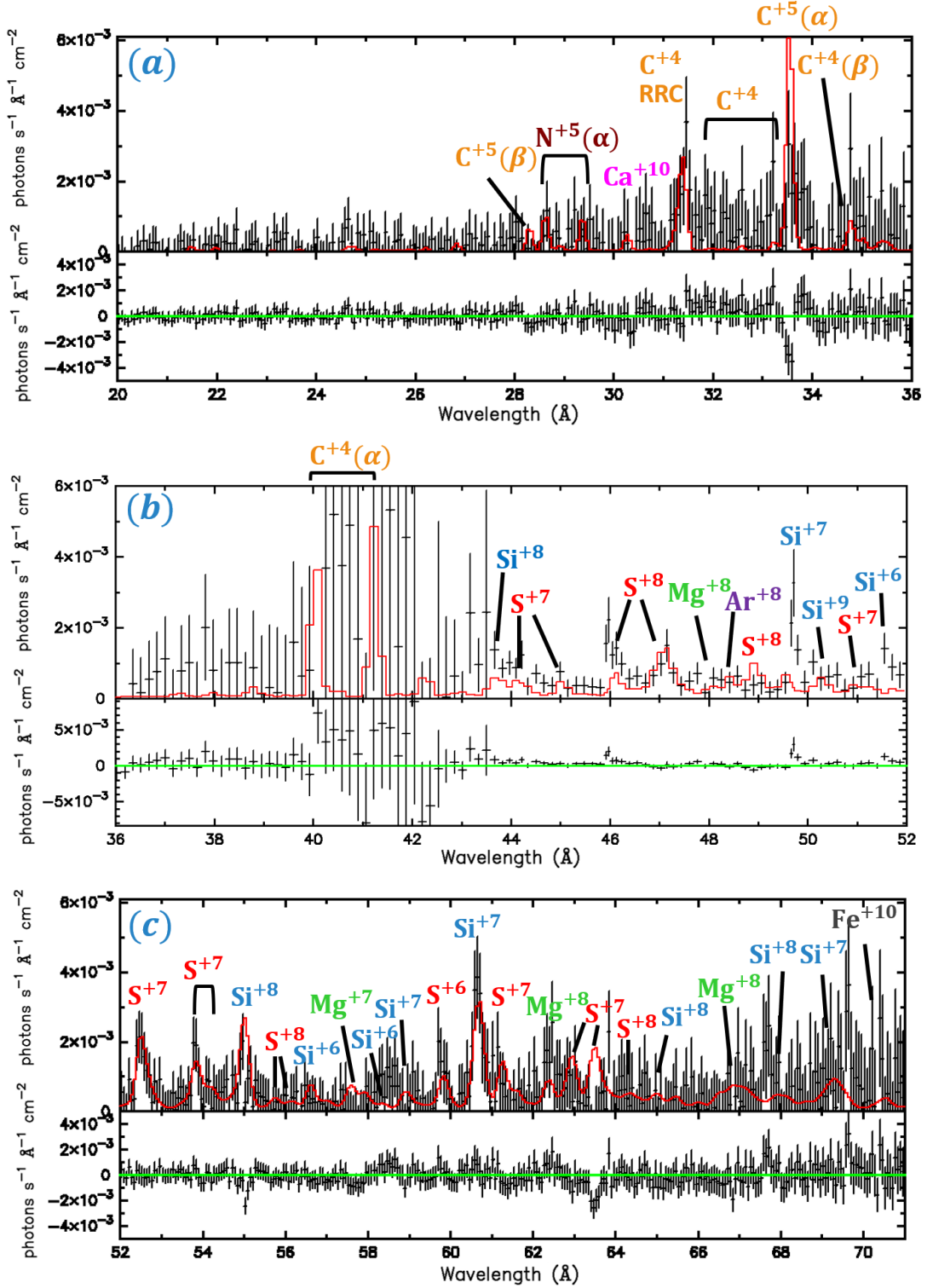


Figure 13. The full spectrum of YZ Ret observed with Chandra and the HRC-I+LETG instrumental setup. The spectrum is presented with the fitted model, the residuals (lower panels) and the identified lines. The cold temperature C⁺⁴ RRC is still visible at 31.5 Å. In panel (b), where the effective area around the carbon edge of the detector is particularly low, the data are rebinned for visual clarity.

6. DISCUSSION

The key diagnostic is the high density $n_e = 10^{11} \text{ cm}^{-3}$, which implies extremely short time scales. For a C^+5 recombination rate coefficient of $\alpha^{RR} \sim 3 \times 10^{-13} \text{ cm}^3 \text{ s}^{-1}$, the recombination (and ionization) time is $\sim 30 \text{ s}$. For a solar abundance plasma at $kT = 70 \text{ eV}$, the cooling function is $\Lambda \simeq 10^{-22} \text{ erg cm}^3 \text{ s}^{-1}$ (Sutherland & Dopita 1993), and thus the radiative cooling time is $\tau = kT/n_e\Lambda \simeq 10 \text{ s}$. The fact that the X-ray source persists on much longer time scales implies continuous heating, which can be attributed to a reverse shock in the nova ejecta. Only the most recently shocked gas remains hot, resulting in a thin X-ray emitting shell, consistent with the theory of Hachisu & Kato (2023). The reverse shock velocity can remain constant for a long time as it moves through the ejecta (Hachisu & Kato 2023), as also expected in supernova remnants (Micelotta et al. 2016, Fig. 4 therein).

If we ascribe a width $\delta r \approx v\tau \approx 10^9 \text{ cm}$ to the shell during the RGS epoch, the thin shell geometry implies $V = \Omega r^2 \delta r$, where Ω is the opening angle of the flow in sr. For $V_{\text{hot}} = 6 \times 10^{35} \text{ cm}^3$; $\Omega r^2 = 6 \times 10^{26} \text{ cm}^2$. From here, the mass outflow rate in the shell is $\dot{M} = \Omega r^2 n v \mu m_p$. Plugging in all the above estimated parameters, we obtain $\dot{M} = 3 \times 10^{-4} M_{\odot} \text{ yr}^{-1}$. Since in this approximation, $\delta r \propto \tau \propto 1/n_e$, as the outflow expands and the density decreases, δr increases. In Section 4.4, we estimated the length scale of mixing between the hot and cold gas to be even smaller than 10^9 cm .

6.1. Shock heating and cooling

Direct evidence for the shocked plasma comes from the line widths. The measured $\sigma_v = 500 \text{ km s}^{-1}$ corresponds to a post-shock C ion ($M_C = 12m_p$) temperature of $kT = 12m_p\sigma_v^2 = 30 \text{ keV}$. The reason we do not observe such high electron temperatures and fully charged ions is a combination of the long electron-ion interaction times, and the efficient electron cooling. At 10^{11} cm^{-3} , electrons would need $\sim 200 \text{ s}$ to reach the ion temperature (Fig. 4.5 in Vink 2020), while their cooling times are tens of seconds.

Assuming 30 keV is the shock temperature kT_s , the relative velocity v_s between the shock and the unshocked ejecta (neglecting radiation losses) is given by $kT_s = (3/16)m_p v_s^2$, or $v_s = 4000 \text{ km s}^{-1}$. The reverse shock is often much slower in the observed frame (Micelotta et al. 2016). Thus, v_s is approximately the velocity of the unshocked ejecta. As expected, it is higher than 1500 km s^{-1} , the velocity of the plasma after it is shocked. The high velocity of 4000 km s^{-1} suggests the ejecta escaped from close to the photosphere of the WD, yet is shocked further out.

6.2. Comparing the two epochs, evidence for a standing shock?

What can we learn from comparing the RGS (day 77) and LETG (day 115) spectra? Both are fitted well with a 70 eV plasma model (*bvapec*). The lines in both are blueshifted by $\sim -1500 \text{ km s}^{-1}$, and broadened by $\sigma_v \sim 500 \text{ km s}^{-1}$. Both spectra feature narrow ($\sim 2 \text{ eV}$) RRCs representing a cold plasma component. However, the X-ray flux on day 115 is about 40 times lower (c.f. Fig. 1), which is approximately true separately for both the hot and recombining components. Table 2 summarizes the important fitted parameters.

If the X-ray source is moving out at 1500 km s^{-1} over these 38 days, it traveled a distance of $5 \times 10^{14} \text{ cm}$. Since the X-rays started to rise ≈ 20 days earlier, by day 77 it could have already reached $\sim 2.5 \times 10^{14} \text{ cm}$. Interestingly, Nova Delphini 2013 was also observed with gratings late (days 87 and 114 there), featuring blueshifted C and N lines, but in absorption with the SSS as a back-lighter (Milla & Paerels 2023). The fast velocities at these late times led those authors as well to explain the absorption by a thin shell ejected early, but now 10^{15} cm away from the center. The X-ray source in YZ Ret seems to be in a similar situation, only the SSS is obscured.

Returning to the conical outflow geometry, and using a distance at the RGS epoch of $r = 2.5 \times 10^{14} \text{ cm}$, and $V_{\text{hot}} = \Omega r^2 \delta r = (6 \pm 3) \times 10^{35} \text{ cm}^3$, we get $\Omega \delta r = (8 \pm 3) \times 10^5 \text{ cm}$. If $\delta r \approx 10^9 \text{ cm}$, it implies a minuscule Ω of $8 \times 10^{-4} \text{ sr}$, namely small and dense blobs of ejecta. If on the other hand $\delta r \approx 10^7 \text{ cm}$ (Sec. 4.4), then $\Omega \sim 8 \times 10^{-2} \text{ sr}$, or a few degrees. At the LETG epoch, the gas expanded by a factor of 3 to $r = 7.5 \times 10^{14} \text{ cm}$. Assuming $\Omega \delta r$ remained the same, given similar cooling times, the corresponding volume on day 115 increased by a factor of 9, $V_{\text{hot}} \propto r^2 = (5 \pm 2) \times 10^{36} \text{ cm}^3$. The day 115 LETG X-ray flux is a factor ~ 40 lower than on day 77. Thus, from Eq. 7, n_e decreased by only a factor of 2, and so did the cooling time, justifying an approximately constant δr .

The continuous shock over 38 days in Sec. 6.2 suggests a large distance from the center, and poses a challenge with its extremely small opening angle Ω . However, a reverse shock does not need to expand so fast, or at all. In a standing shock, the ejecta flows from the center at several 1000 km s^{-1} , collides with the shock front, and exits the shock region at 1500 km s^{-1} (see Sec. 6.1 for the velocity and temperature estimates), while the shock location remains constant in the observer's frame of reference. Since the cooling time is short, we observe fresh (recently) shocked ejecta at each

time. The fact that the temperature and velocity broadening are similar after 38 days, attests to the constant relative velocities of the ejecta and the shock over this long time scale. In this scenario, the X-ray flux variability in Fig. 1 can be ascribed to the varying mass outflow rate of the nova. A factor of 40 fainter X-rays with LETG compared to the RGS, thus indicates a similar factor reduction in the density, from 10^{11} cm^{-3} to a few 10^9 cm^{-3} . For a standing shock unfortunately, we have no distance diagnostics. In the thin shell geometry, a location closer to the center implies a larger opening angle, since the measured volume is $V \propto \Omega r^2$. If, say, $\Omega \sim 1 \text{ sr}$, with $\delta r \sim 10^9 \text{ cm}$, it would imply a distance of $r = \text{few} \times 10^{13} \text{ cm}$, and higher for smaller δr .

6.3. The Cool Plasma Component

The outflow velocity and the volume estimates of the cold plasma (2 eV from the RRCs) are almost identical to that of the hot plasma, which suggests the two components are physically connected. This is not the first time narrow RRCs are observed in shocked X-ray sources. Schild et al. (2004) found C^{+4} and C^{+5} RRCs in the RGS spectrum of the colliding wind binary $\gamma^2 \text{ Vel}$, which indicate a temperature of 40kK (few eV) in a hot (keV) plasma. Nordon et al. (2009) analyzed the C^{+5} RRC in the LETG spectrum of the planetary nebula BD+30°3639, and found a temperature of $kT_e = 1.7 \pm 1.3 \text{ eV}$ in a hot 160-260 eV plasma. These RRCs were unambiguously detected in high-resolution grating spectra. Fe^{+24} and Fe^{+25} RRCs were detected with the *Suzaku* CCDs in supernova remnants (Ozawa et al. 2009; Yamaguchi et al. 2009) at much higher temperatures of $kT \simeq 1 \text{ keV}$. All of these findings combined suggest that narrow RRCs are a common feature of shocked plasmas.

The physical origin of these RRCs and the source of cold electrons are debated. While adiabatic cooling and ionization freezing has been proposed (Schild et al. 2004; Yamaguchi et al. 2009), we suspect there is genuine mixing of cold electrons with the highly-charged ions. Mixing with cold gas can occur either at the reverse-shock front between shocked and unshocked wind, or at the contact discontinuity, at the interface between shocked ejecta and the dense, much cooler, shocked ISM gas. Computing the penetration depth of 2 eV electrons into the hot gas region, by taking the Larmor radius in a $1 \mu\text{G}$ magnetic field, one gets $R_L \simeq 5 \times 10^6 \text{ cm}$, which is comparable to the hot thin shell size estimated in Sec. 4.4. Neutral atoms from the cold phase of course penetrate the hot gas smoothly, with no magnetic obstacle. These neutrals are discussed in Sec. 4.2. Another possible scenario is runaway radiative cooling. The cooling function of astrophysical plasmas peaks sharply at $\Lambda \approx 10^{21} \text{ erg cm}^3 \text{ s}^{-1}$ between $4.2 \text{ K} < \log T < 5.7 \text{ K}$ (e.g., Sutherland & Dopita 1993). This implies that gas cooling below $\sim 50 \text{ eV}$ would rapidly cool down to 1-2 eV. At the density of 10^{11} cm^{-3} this cooling time is $\tau < 1 \text{ s}$. This could explain why we observe narrow RRCs, namely no gas whatsoever at temperatures above 2 eV.

The X-ray source in YZRet is exceptional in its high density, small volume, and prominent RRCs. We suspect that under these conditions, the highly charged ions are completely immersed in the dense cold gas, the source of which could be one of the above. Another source of cold material could be an accretion disk. Ness et al. (2013) suggested that X-ray emission line spectra observed with no SSS after nova eruptions originate in high-inclination systems, where the SSS is obscured by optically thick material, formed in a disk around it. This disk can explain the lack of an observed SSS in YZRet, and provide a cold dense medium that the shocked gas runs into to produce the observed narrow RRCs and the CX. However, since the RRCs and high- n lines are blueshifted, the wind would need to carry cool disk material with it without slowing down. The geometry and inclination of the system would need to be fine tuned to completely hide the WD, but allow us to still observe the approaching wind interacting with the edge of the disk.

7. CONCLUSIONS

We observed nova YZRet 2020 77 and 115 days after the eruption with *XMM-Newton* and *Chandra* gratings, respectively. The X-ray flux decreased by a factor of ~ 40 between epochs. Both X-ray spectra are characterized by emission lines with no sign of thermal emission from the SSS. In the following we summarize our conclusions from the analysis of the two spectra:

1. Three totally different density diagnostics, namely using $f/i = 1.1 \pm 0.1$ in He-like N (Sec. 4.3), $n_{\text{max}} = 35_{-5}^{+10}$ in the $1s_{nl}$ Rydberg series of He-like C (Sec. 4.1), and $1s_{n'l'}$ satellite line ratios of He-like C (Sec. 4.4), all point to $n_e \simeq 10^{11} \text{ cm}^{-3}$.
2. This key density diagnostic indicates radiative cooling and recombination times of the order of tens of seconds, which must imply ongoing heating, ascribed to a thin shock-heated layer of $10^7 - 10^9 \text{ cm}$ in the nova ejecta (Sections 4.4, 6).

3. The emission lines originate in collisionally ionized plasma of $kT_e \simeq 70$ eV that was heated by the shock (Sec. 5), but may not have had time to reach its maximal temperature or ionization degree due to the rapid radiative cooling. The $\sigma_v = 500$ km s⁻¹ broadened lines suggest the ions may still be hot at $kT \sim 30$ keV.
4. The narrow RRCs in the spectrum indicate the presence of cold 2 eV electrons, recombining with the hot, highly-charged C and N ions (Sec. 4.1). These cold electrons could have crossed into the shocked region via the contact discontinuity, or the shock front (Sec. 6.3).
5. The DR satellite line observed at 33.87 Å (rest frame) indicates a close interaction between the hot (70 eV) and cold (2 eV) components via photo-pumping. The high photon flux that is needed to produce the observed satellite line ratios implies the two are mixed (Sec. 4.4).
6. The high- n Rydberg series of C⁺⁴ suggests highly charged ions are undergoing CX with neutral atoms, furthering the evidence for mixing of shocked and cold gas in the nova.

The consistently high outflow velocity of -1500 km s⁻¹ over 38 days would imply a source size of $\sim 10^{15}$ cm (Sections 4.5, 6.1), but an outflow with a disturbingly minuscule opening angle, consistent maybe with small dense blobs and a low volume filling factor. Conversely, invoking a standing reverse shock could imply a shorter distance, and thus alleviate the small opening angle problem.

S.M. and E.B. were supported in part by a Center of Excellence of the Israel Science Foundation (grant No. 1937/19). M.O. was supported by a Chandra-Smithsonian award for the *Chandra*/LETG observation. This paper employs a list of Chandra datasets, obtained by the Chandra X-ray Observatory, contained in the Chandra Data Collection (CDC) 233 [doi:10.25574/cdc.233](https://doi.org/10.25574/cdc.233)

REFERENCES

- Arnaud, K. A. 1996, in *Astronomical Society of the Pacific Conference Series*, Vol. 101, *Astronomical Data Analysis Software and Systems V*, ed. G. H. Jacoby & J. Barnes, 17
- Aydi, E., Buckley, D. A. H., Chomiuk, L., et al. 2020, *The Astronomer’s Telegram*, 13867, 1
- Aydi, E., Chomiuk, L., Strader, J., et al. 2023, arXiv e-prints, arXiv:2309.07097, doi: [10.48550/arXiv.2309.07097](https://doi.org/10.48550/arXiv.2309.07097)
- Bailer-Jones, C. A. L., Rybizki, J., Fouesneau, M., Demleitner, M., & Andrae, R. 2021, *AJ*, 161, 147, doi: [10.3847/1538-3881/abd806](https://doi.org/10.3847/1538-3881/abd806)
- Bailer-Jones, C. A. L., Rybizki, J., Fouesneau, M., Demleitner, M., & Andrae, R. 2021, *The Astronomical Journal*, 161, 147, doi: [10.3847/1538-3881/abd806](https://doi.org/10.3847/1538-3881/abd806)
- Bar-Shalom, A., Klapisch, M., & Oreg, J. 2001, *JQSRT*, 71, 169, doi: [10.1016/S0022-4073\(01\)00066-8](https://doi.org/10.1016/S0022-4073(01)00066-8)
- Brinkman, A. C., Gungasing, C. J. T., Kaastra, J. S., et al. 2000, *ApJL*, 530, L111, doi: [10.1086/312504](https://doi.org/10.1086/312504)
- Burrows, D. N., Hill, J. E., Nousek, J. A., et al. 2005, *SSRv*, 120, 165, doi: [10.1007/s11214-005-5097-2](https://doi.org/10.1007/s11214-005-5097-2)
- Cann, N. M., & Thakkar, A. J. 1992, *Phys. Rev. A*, 46, 5397, doi: [10.1103/PhysRevA.46.5397](https://doi.org/10.1103/PhysRevA.46.5397)
- Carr, A., Said, K., Davis, T. M., Lidman, C., & Tucker, B. E. 2020, *The Astronomer’s Telegram*, 13874, 1
- Chomiuk, L., Metzger, B. D., & Shen, K. J. 2021, *ARA&A*, 59, 391, doi: [10.1146/annurev-astro-112420-114502](https://doi.org/10.1146/annurev-astro-112420-114502)
- den Herder, J. W., Brinkman, A. C., Kahn, S. M., et al. 2001, *A&A*, 365, L7, doi: [10.1051/0004-6361:20000058](https://doi.org/10.1051/0004-6361:20000058)
- Dewey, J. M., & Robertson, H. P. 1928, *Nature*, 121, 709, doi: [10.1038/121709b0](https://doi.org/10.1038/121709b0)
- Drake, G. W. F. 1969, *ApJ*, 158, 1199, doi: [10.1086/150279](https://doi.org/10.1086/150279)
- Drake, G. W. F. 1971, *Phys. Rev. A*, 3, 908, doi: [10.1103/PhysRevA.3.908](https://doi.org/10.1103/PhysRevA.3.908)
- Drake, J. J., Delgado, L., Laming, J. M., et al. 2016, *ApJ*, 825, 95, doi: [10.3847/0004-637X/825/2/95](https://doi.org/10.3847/0004-637X/825/2/95)
- Franckowiak, A., Jean, P., Wood, M., Cheung, C. C., & Buson, S. 2018, *A&A*, 609, A120, doi: [10.1051/0004-6361/201731516](https://doi.org/10.1051/0004-6361/201731516)
- Gabriel, A. H., & Jordan, C. 1969, *Monthly Notices of the Royal Astronomical Society*, 145, 241, doi: [10.1093/mnras/145.2.241](https://doi.org/10.1093/mnras/145.2.241)
- Hachisu, I., & Kato, M. 2023, *ApJ*, 953, 78, doi: [10.3847/1538-4357/acdfd3](https://doi.org/10.3847/1538-4357/acdfd3)
- Hessman, F. V. 2000, *NewAR*, 44, 155, doi: [10.1016/S1387-6473\(00\)00030-0](https://doi.org/10.1016/S1387-6473(00)00030-0)
- Honeycutt, R. K., & Kafka, S. 2004, *AJ*, 128, 1279, doi: [10.1086/422737](https://doi.org/10.1086/422737)
- Inglis, D. R., & Teller, E. 1939, *ApJ*, 90, 439, doi: [10.1086/144118](https://doi.org/10.1086/144118)

- Islam, N., & Mukai, K. 2023, in AAS/High Energy Astrophysics Division, Vol. 55, AAS/High Energy Astrophysics Division, 116.60
- Izzo, L., Molaro, P., Aydi, E., et al. 2020, *The Astronomer's Telegram*, 14048, 1
- Janev, R., & Winter, H. 1985, *Physics Reports*, 117, 265, doi: [https://doi.org/10.1016/0370-1573\(85\)90118-8](https://doi.org/10.1016/0370-1573(85)90118-8)
- Kalberla, P. M. W., Burton, W. B., Hartmann, D., et al. 2005, *A&A*, 440, 775, doi: [10.1051/0004-6361:20041864](https://doi.org/10.1051/0004-6361:20041864)
- Kallman, T. R., Bautista, M. A., Goriely, S., et al. 2009, *ApJ*, 701, 865, doi: [10.1088/0004-637X/701/2/865](https://doi.org/10.1088/0004-637X/701/2/865)
- Kaufman, R., McNaught, R. H., Phillips, M. A., et al. 2020, *Central Bureau Electronic Telegrams*, 4812, 1
- King, A. R., & Cannizzo, J. K. 1998, *ApJ*, 499, 348, doi: [10.1086/305630](https://doi.org/10.1086/305630)
- Kinkhabwala, A., Sako, M., Behar, E., et al. 2002, *ApJ*, 575, 732, doi: [10.1086/341482](https://doi.org/10.1086/341482)
- König, O., Wilms, J., Arcodia, R., et al. 2022, *Nature*, 605, 248, doi: [10.1038/s41586-022-04635-y](https://doi.org/10.1038/s41586-022-04635-y)
- Leahy, D., Foster, A., & Seitzzahl, I. 2023, arXiv e-prints, arXiv:2311.11181, doi: [10.48550/arXiv.2311.11181](https://doi.org/10.48550/arXiv.2311.11181)
- Liedahl, D. A., & Paerels, F. 1996, *ApJL*, 468, L33, doi: [10.1086/310217](https://doi.org/10.1086/310217)
- Livio, M., & Pringle, J. E. 1994, *ApJ*, 427, 956, doi: [10.1086/174202](https://doi.org/10.1086/174202)
- Lotz, W. 1968, *Zeitschrift für Physik*, 216, 241, doi: [10.1007/BF01392963](https://doi.org/10.1007/BF01392963)
- Micelotta, E. R., Dwek, E., & Slavin, J. D. 2016, *A&A*, 590, A65, doi: [10.1051/0004-6361/201527350](https://doi.org/10.1051/0004-6361/201527350)
- Milla, J., & Paerels, F. 2023, *ApJ*, 943, 31, doi: [10.3847/1538-4357/aca966](https://doi.org/10.3847/1538-4357/aca966)
- Mitrani, S., & Behar, E. 2023, *ApJ*, 957, 105, doi: [10.3847/1538-4357/acf562](https://doi.org/10.3847/1538-4357/acf562)
- Ness, J. U., Starrfield, S., Burwitz, V., et al. 2003, *ApJL*, 594, L127, doi: [10.1086/378664](https://doi.org/10.1086/378664)
- Ness, J. U., Osborne, J. P., Henze, M., et al. 2013, *A&A*, 559, A50, doi: [10.1051/0004-6361/201322415](https://doi.org/10.1051/0004-6361/201322415)
- Nolte, J. L., Stancil, P. C., Liebermann, H. P., et al. 2012, *Journal of Physics B Atomic Molecular Physics*, 45, 245202, doi: [10.1088/0953-4075/45/24/245202](https://doi.org/10.1088/0953-4075/45/24/245202)
- Nordon, R., Behar, E., Soker, N., Kastner, J. H., & Yu, Y. S. 2009, *ApJ*, 695, 834, doi: [10.1088/0004-637X/695/2/834](https://doi.org/10.1088/0004-637X/695/2/834)
- Orio, M. 2012, *Bulletin of the Astronomical Society of India*, 40, 333, doi: [10.48550/arXiv.1210.4331](https://doi.org/10.48550/arXiv.1210.4331)
- Orio, M., Drake, J. J., Ness, J. U., et al. 2020, *ApJ*, 895, 80, doi: [10.3847/1538-4357/ab8c4d](https://doi.org/10.3847/1538-4357/ab8c4d)
- Orio, M., Gendreau, K., Giese, M., et al. 2022, *ApJ*, 932, 45, doi: [10.3847/1538-4357/ac63be](https://doi.org/10.3847/1538-4357/ac63be)
- . 2023, *ApJ*, 955, 37, doi: [10.3847/1538-4357/ace9bd](https://doi.org/10.3847/1538-4357/ace9bd)
- Ozawa, M., Koyama, K., Yamaguchi, H., Masai, K., & Tamagawa, T. 2009, *ApJL*, 706, L71, doi: [10.1088/0004-637X/706/1/L71](https://doi.org/10.1088/0004-637X/706/1/L71)
- Peretz, U., Orio, M., Behar, E., et al. 2016, *ApJ*, 829, 2, doi: [10.3847/0004-637X/829/1/2](https://doi.org/10.3847/0004-637X/829/1/2)
- Schild, H., Güdel, M., Mewe, R., et al. 2004, *A&A*, 422, 177, doi: [10.1051/0004-6361:20047035](https://doi.org/10.1051/0004-6361:20047035)
- Seely, J. F., Dixon, R. H., & Elton, R. C. 1981, *PhRvA*, 23, 1437, doi: [10.1103/PhysRevA.23.1437](https://doi.org/10.1103/PhysRevA.23.1437)
- Shen, K. J., & Quataert, E. 2022, *ApJ*, 938, 31, doi: [10.3847/1538-4357/ac9136](https://doi.org/10.3847/1538-4357/ac9136)
- Smith, R. K., Brickhouse, N. S., Liedahl, D. A., & Raymond, J. C. 2001, *ApJL*, 556, L91, doi: [10.1086/322992](https://doi.org/10.1086/322992)
- Sokolovsky, K. V., Li, K.-L., Lopes de Oliveira, R., et al. 2022, *MNRAS*, 514, 2239, doi: [10.1093/mnras/stac1440](https://doi.org/10.1093/mnras/stac1440)
- Starrfield, S., Iliadis, C., Timmes, F. X., et al. 2012, *Bulletin of the Astronomical Society of India*, 40, 419, doi: [10.48550/arXiv.1210.6086](https://doi.org/10.48550/arXiv.1210.6086)
- Sutherland, R. S., & Dopita, M. A. 1993, *ApJS*, 88, 253, doi: [10.1086/191823](https://doi.org/10.1086/191823)
- Vink, J. 2020, *Shocks and Post-shock Plasma Processes* (Cham: Springer International Publishing), 55–85, doi: [10.1007/978-3-030-55231-2_4](https://doi.org/10.1007/978-3-030-55231-2_4)
- Williams, R. E. 1992, *AJ*, 104, 725, doi: [10.1086/116268](https://doi.org/10.1086/116268)
- Wilms, J., Allen, A., & McCray, R. 2000, *ApJ*, 542, 914, doi: [10.1086/317016](https://doi.org/10.1086/317016)
- Wolf, W. M., Bildsten, L., Brooks, J., & Paxton, B. 2013, *ApJ*, 777, 136, doi: [10.1088/0004-637X/777/2/136](https://doi.org/10.1088/0004-637X/777/2/136)
- Wu, K., Wickramasinghe, D. T., & Warner, B. 1995, *PASA*, 12, 60, doi: [10.1017/S13233580002004X](https://doi.org/10.1017/S13233580002004X)
- Yamaguchi, H., Ozawa, M., Koyama, K., et al. 2009, *ApJL*, 705, L6, doi: [10.1088/0004-637X/705/1/L6](https://doi.org/10.1088/0004-637X/705/1/L6)
- Yaron, O., Prialnik, D., Shara, M. M., & Kovetz, A. 2005, *ApJ*, 623, 398, doi: [10.1086/428435](https://doi.org/10.1086/428435)
- Zemko, P., Orio, M., Mukai, K., & Shugarov, S. 2014, *MNRAS*, 445, 869, doi: [10.1093/mnras/stu1783](https://doi.org/10.1093/mnras/stu1783)